

Application of boundary layer wind-profiling radar data to a Springtime Snowstorm Analysis in Urumqi

Wang Minzhong,^{a,b*} Wei Wenshou,^a He Qing,^{a,b} Yang Qing,^{a,b} Zhao Yong,^{a,b} Li Hongjun^{a,b} and Huo Wen^{a,b}

^a Institute of Desert Meteorology, CMA (China Meteorological Administration), Urumqi, Xinjiang, China

^b Taklimakan Desert Atmospheric Environment Observation Experimental Station, Tazhong, Xinjiang, China

ABSTRACT: The Urumqi Institute of Desert Meteorology under the China Meteorological Administration (CMA) launched an observational experiment with a boundary layer wind-profiling radar in Urumqi City in February to March 2010. As described in this paper, wind profiles from the experiment were used to first compare with radiosonde data measured simultaneously to verify the confidence of wind-profiling radar data, which was used to analyse the wind field characteristics and other related issues in a snowstorm process that took place in Urumqi on 28 March 2010. Both wind direction and speed derived from wind-profiling radar data have good consistency with those from radiosonde data (wind velocity coefficient: 0.85; wind direction coefficient: 0.78). Before the snowstorm, a surface wind shear occurred. After outbreak of the event, the local weather was dominated by northwesterly and northerly winds at increasing velocities, while temperature was dropping and air pressure increased. Through in-depth analyses of the time-height profiles of the snowstorm process, it can be determined on a preliminary basis that the snowstorm was induced by a cold front system that entered the area around 2200–2300 LST on 27 March. A shear line that developed from a lower to a higher altitude represented both height and location of the frontal zone, and the cold front motion was broadly in a northeast-southwest direction. The wind direction in the process changed counterclockwise with height: this was mainly governed by cold advection, and baroclinic instability was established soon after the overpass of the cold front, eventually leading to the snowstorm. During the weather event, the equivalent reflectivity factor Z_e was consistent with the onset and end of the snowstorm, the height at which rain (snow) particles were formed and snowfall intensity. Copyright © 2011 Royal Meteorological Society

KEY WORDS wind-profiling radar; snowstorm; cold front system; thermal advection; equivalent reflectivity factor Z_e

Received 31 March 2011; Revised 23 July 2011; Accepted 4 August 2011

1. Introduction

Wind-profiling radar (WPR) is an emerging remote sensing system for upper air observations developed in the 1970s. Through further improvements in the past 30 years, WPR technology is now mature (He *et al.*, 2010). For decades both national and international scientific communities have done tremendous work on atmospheric wind field and gravity wave observations (Balsley *et al.*, 1988; Angevine, 1997; May and Rajopadhyaya, 1999; Lothon *et al.*, 2002; Vaughan and Worthington, 2007; Xin *et al.*, 2009), numerical weather predictions (Kuo *et al.*, 1987), precipitation processes (Fukao *et al.*, 1985; Larsen and Rottger, 1987; Chilson *et al.*, 1993; Ralph, 1995; Gage *et al.*, 1996; Cifelli and Rutledge, 1998; Rao *et al.*, 1999; Deshpande and Raj, 2009), measurement of atmospheric turbulences and boundary layer thickness (Balsley and Peterson, 1981; Hocking, 1983; Hocking, 1985; Angevine *et al.*, 1994; Hashiguchi *et al.*, 1996; Gossard *et al.*, 1998; Hermawan and Tsuda, 1999), detection of bright band at 0°C level (Austin and Bemis, 1950; Cheng and Collier, 1993; Borga *et al.*, 1997), and inversion of droplet size distribution (Wakasugi *et al.*, 1986; Currier *et al.*, 1992; Maguire and Avery, 1994) by using WPR radars, and so far substantive encouraging findings have been made available. As a new generation atmospheric remote sensing instrument,

WPRs have been networked and used for operational meteorology in the United States, Japan and other countries. The National Oceanic and Atmospheric Administration (NOAA) deployed 35 WPR radars in the central and southern U.S. in 1987–1992, providing WPR observations for NWS centres, environmental research institutions and universities (Orr and Martner, 1996). The operational use of WPRs for nearly 20 years shows that WPR has a stronger capability to detect 3-D wind fields in the atmosphere, and its refined vertical profiles reveal continuous and detailed evolution of such weather systems as fronts, short-wave turbulences, cyclones and gravity waves, which have significantly improved the quality of severe weather forecasts (Barth *et al.*, 1994).

Since the 1980s, China has been involved in WPR development and applications. In 1989, the Chinese Academy of Meteorological Sciences developed its first UHF band wind-filing radar for operational experiments at the Beijing Meso-scale Severe Weather Forecast Base, having proved its effectiveness and reliability (He, 2006). In the past decade, China has made significant progress in WPR manufacturing technologies. WPR hardware performance has evolved, with a number of technical functions being comparable with the world advanced level. A variety of WPRs have been developed independently and developed for both operational uses and research work (He *et al.*, 2010). Using WPRs, Zou *et al.* (2007) and Wang *et al.* (2010) made observational studies on 3-D wind fields in Rongbu Valley to the north of Mt Everest in one case and in the windy zone of Xinjiang AR in another. Ruan *et al.* (2002) analysed cloud

* Correspondence to: W. Minzhong, Institute of Desert Meteorology, CMA (China Meteorological Administration), Urumqi 830002, Xinjiang, China. E-mail: yurenkeji@sina.com

and rainfall vertical structures and their evolution by measuring the signal power from WPR echoes. Gu *et al.* (1993) used WPR data from Beijing to analyse local heavy rainfalls and frontal processes, showing the promising applicability of WPR in short-range weather forecasts. He *et al.* (2009) analysed the characteristics of wind profiles in a precipitation process over the Yanqing area of Beijing and concluded that the wind profiles could capture changes in large-scale air flow fields in a timely manner, which are applicable to precipitation forecasts. All these studies show the important role of WPR in weather monitoring, especially in wind field detection, and studies of clouds and precipitation.

As a severe weather event, a snowstorm is an important weather process that often leads to snow-related hazards. For a long time, meteorologists have made extensive and in-depth studies on snowstorm weather (Bendel and Paton, 1981; Braham, 1983; Chen *et al.*, 1999; Zhou *et al.*, 2000; Wang *et al.*, 2008). However, there are few studies on snowstorms by using WPR radar both in China and overseas. The Urumqi Institute of Desert Meteorology launched an experiment on snowstorms by using WPR radar at the Tianshan District Meteorological Bureau of Urumqi City (43°47'N, 87°39'E, elevation: 936 m) from 1 February to 30 March 2010. This experiment provided such meteorological data as horizontal wind speed and direction, vertical velocity and the turbulence refractive index structure constant (C_n^2) within the 50–4000 m height range. In this paper, wind profiles are first compared with *in situ* radiosonde data observed at the same time, to verify the WPR data. WPR data are then used to analyse wind field characteristics and relevant issues in a snowstorm which occurred during the experiment, with a view to applying WPR data to weather analyses and forecasts in the Xinjiang region.

2. Basic principles and major technical performance of CFL-03 wind-profiling radar detection

Turbulences on different scales in the atmosphere change over time, which leads to irregular variations of refractivity index and scatter radar waves. Wind-profiling radar emits radio waves, and receives echoes, which are the radio wave refractions from atmospheric turbulence at different levels. Through radar echo processing and analysis, Doppler wind and intensity coefficients of an atmospheric turbulence are established to derive turbulent intensity, air motion direction and speed distribution with height. Atmospheric turbulence is driven by background wind motions and atmospheric instability. Therefore, if Doppler speed and direction of atmospheric turbulence are captured, the wind speed and directions can be obtained simultaneously (Zhang *et al.*, 2004).

The equipment used for this study is CFL-03 phased array wind-profiling radar, developed by the 23rd Institute of China Aerospace Science and Industry Corporation (Figure 1), which has six components: antenna feeder, transmitter, receiver, monitoring system, signal processing and control, and data processing system. With a designed detection height of 3000–5000 m, it falls into the category of boundary layer wind-profiling radars. Compared with Doppler weather radars, CFL-03 adopts a phased array antenna system, and its beam formation, beam pointing and scanning are more accurate and faster. It can detect scattered signals both from atmospheric turbulences and precipitation particles. The CFL-03 radar adopts a detection approach by transmitting five fixed-direction beams, i.e. one vertical beam and four tilt beams at a zenith angle of 15°. These tilt beams are evenly and orthogonally distributed across



Figure 1. CFL-03 mobile boundary layer wind-profiling radar system. This figure is available in colour online at wileyonlinelibrary.com/journal/met

azimuth. To keep a balance between the detection height and resolution at lower levels, CFL-03 runs in both high and low operating modes. The former uses a wider pulse with spatial resolution of 100 m, while the latter uses a narrower pulse with a 50 m resolution, with a temporal resolution of 3 min. These two modes switch alternately to ensure a higher resolution for detections at low levels while reaching a higher detection height almost at the same time. The data format provided by CFL-03 radar fully meets the CMA criteria for spectrum data, radial spectrum velocity and real-time profile in high/low mode. Each profile contains such information as horizontal wind, vertical velocity, signal to noise ratio, the turbulence refractive index structure constant (C_n^2), and spectral width. Table 1 lists the main technical parameters of the CFL-03 wind-profiling radar. Its high spatial and temporal resolutions are particularly suitable for detections of small- and meso-scale weather phenomena and processes. Besides, its fine vertical profiles can describe in more details the vertical structure of weather processes, and their evolution.

3. Analysis of inter-comparison experiment

To verify the reliability of WPR data, comparative observations were made with both wind-profiling radar and a radiosonde system (type 701 secondary wind-finding radar) at the same time at the Tianshan District Meteorological Bureau between 10 and 20 February 2010.

The Tianshan District Meteorological Bureau in Urumqi City makes radiosonde observations twice a day, at 0715 and 1915 Beijing time respectively (Beijing time = UT + 8 h and is used in this paper). The wind-profiling radar operates continuously for all-weather observations at 6 min intervals. This paper uses the radiosonde data observed simultaneously for making comparative analysis. As radiosondes measure continuous atmospheric status within a given period, while the wind-profiling radar provides instantaneous data in 3 min intervals for sake of inter-comparisons, the hourly comparison shows most recent 3–4 radar observations made before and after a radiosonde balloon was released, and the mean value approximately represents the atmospheric conditions at the time of a radiosonde observation. Figure 2 gives the curves of wind speed and direction from three WPR measurements compared with radiosondes during the observation period (other comparative figures omitted). The analysis shows that the WPR data are broadly consistent with the radiosonde measurements of wind

Table 1. Technical parameters of the CFL-03 wind-profiling radar.

Item	Parameter	Item	High mode parameter	Low mode parameter
Radar wavelength	227 mm	Pulse width	0.66 μ s	0.33 μ s
Beam width	8°	Minimum detection altitude	600 m	50 m
Beam number	5	Noise coefficient	2 dB	2 dB
Antenna gain	25 dB	Height resolution	100 m	50 m
Feeder loss	2 dB	Coherent accumulation number	64	100
Receiver	Digital IF	FFT points	512	256
Transmitting peak power	2.36 KW	Bandwidth	1.5 MHz	3.0 MHz

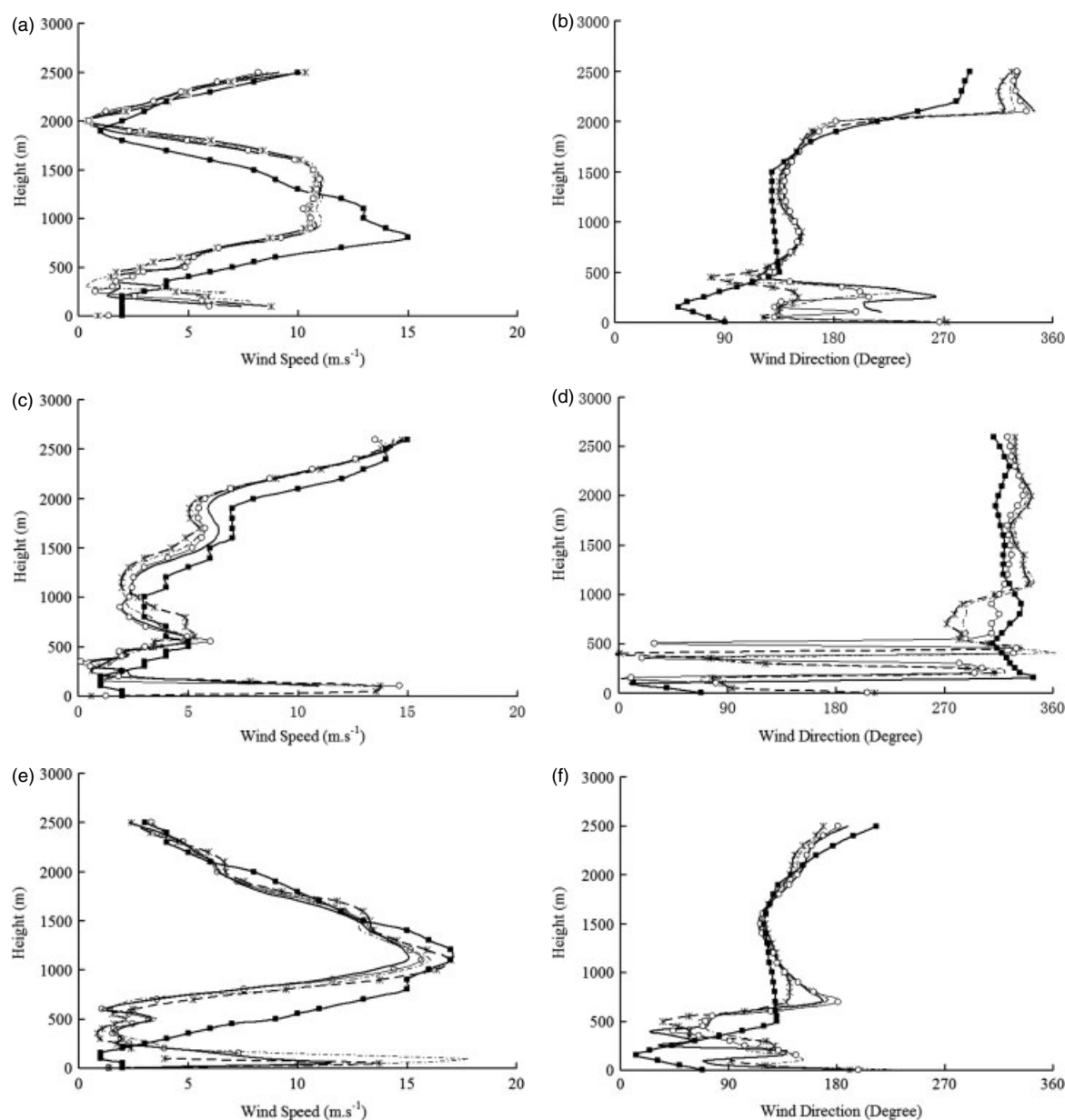


Figure 2. Comparison of wind component measurements from the WPR and radiosonde at Tianshan District Meteorological Bureau in Urumqi. (a) 0715 on 11 February 2010 (b) 0715 on 11 February 2010 (c) 1915 on 14 February 2010 (d) 1915 on 14 February 2010 (e) 1915 on 17 February 2010 (f) 1915 on 17 February 2010. —x—, 0712; ---, 0718; —o—, 0724; —, 0730; —■—, radiosonde; —x—, 1912; ---, 1918; —o—, 1924; —, 1930; —■—, radiosonde.

directions and speeds. The average correlation coefficient for wind speeds measured by the two instruments is 0.85, and that for wind directions is 0.78, demonstrating that WPR wind field data have a good confidence.

4. A brief description of the snowstorm process

Between 0416 and 1640 on 28 March 2010, a snowstorm occurred in Urumqi, during which sleet was observed from

0416 to 0718, followed by snowfall after 0718 until 1640, and the daily precipitation was 12.7 mm in total.

4.1. Upper-air and low-level circulation patterns

On the 500 hPa chart, two ridges and one trough appeared in the Eurasia domain at 0800 on 26 March, in which western Europe and Xinjiang were dominated by the high pressure ridges, and the Urals was controlled by a large trough with its centre located in vicinity of Novaya Zemlya and the trough bottom protruding to central Asia. At about 0800 on 27 March, as the system moved east, a ridge developed over the northern Caspian Sea. In front of the ridge a northerly wind belt was established, driving the cold air southwards continuously. The cold air mass was accumulated in a region from the Aral Sea to Lake Balkhash: eventually, a cold -40°C centre took shape. At around 0800 on 28 March (Figure 3), the cold air began to move south from Novaya Zemlya, forcing the ridge to the north of the Aral Sea to retreat southeast and pushing the trough into Xinjiang. Eventually, this process led to the snowstorm in the Urumqi area.

The trough location on the 700 hPa chart was consistent with that at the 500 hPa level. At 0800 on 27 March, a trough-line was located between the Aral Sea and Lake Balkhash, and a cold centre (-24°C) existed between the Ural Mountains. Strong wind was detected at the trough bottom level, a condition that was favourable for water vapour transport. At 2000 on the same day, northern Xinjiang was dominated by a strong southwesterly wind, whereas there was a wind shear along the Tianshan Mountains. At 0800 on 27 March, from the 850 hPa chart, a trough was located closer to Xinjiang compared with its location further away from it at the 700 hPa level. This suggested that a backward-tilting trough was extending from 500 hPa down to the 850 hPa level. Such a trough usually moves slowly and it has persistent and intensive impacts, which are often conducive to heavy snow events.

Judging from the surface weather charts, at 0800 on 26 March, the weather in Xinjiang was fine under the Mongolian High, and a high-pressure centre existed over the northern Black Sea at the 1032.5 hPa level. As the system developed and moved east from 1400 onwards on 27 March, this centre approached to the Aral Sea area with its central pressure increased to 1040 hPa. At 0200 on 28 March, the high-pressure centre approached Lake Balkhash, with its central pressure reaching 1045 hPa, only a 40 hPa difference from the trough

centre just in front of Xinjiang. Such a strong pressure gradient provided the condition for the eventual outbreak of the snowstorm.

4.2. Changes of surface weather elements in the snowstorm process

Figure 4 shows variation curves of surface air temperature, relative humidity, air pressure, wind speed and direction during the snowstorm that took place in Urumqi in 27–28 March 2010. As shown in this figure, the temperature on 27 March was like a normal diurnal variation. From 0000 to 0800, it was about 0°C and it normally began to rise after 1000, reaching its maximum at 7.7°C at around 1700, followed by a temperature drop. On 28 March, when the snowstorm occurred, the temperature dropped rapidly, maintaining at -4°C during the whole snowstorm process. From the relative humidity curve, it is clear that between 1200 and 1800 on 27 March the relative humidity was lower. However, when the weather system arrived the relative humidity increased rapidly, keeping at around 90% during the whole process, indicating that the heavy snow had brought abundant moisture. As for air pressure, before the snowstorm, it changed smoothly down to 910 hPa, but with invasion of the cold frontal system the pressure gradually increased from 0000 on 28 March, reaching 929.5 hPa at 2200 on the same day. On 27 March, the average wind speed was 1.8 m s^{-1} , which increased up to 2.5 m s^{-1} during the snowstorm. Soon after the snowstorm, it was weakening. The curve of wind direction showed that easterly and northeasterly winds prevailed over Urumqi on 27 March 2010. When the snowstorm began at 0430 on 28 March, the surface wind direction soon changed from northeasterly to northwesterly, as the snowstorm process was dominated by the northwesterly and northerly winds. After the snowstorm, the direction returned to northeasterly. Overall, the above analysis suggested that surface wind shear existed before the snowstorm: at its onset the northwesterly and northerly winds prevailed. During the process, the wind speed and relative humidity were comparatively higher, air temperature dropped and air pressure was on rise.

5. Application analysis

5.1. Application of horizontal wind field data

By analysing the vertical and temporal discontinuity of the wind profiles, the frontal nature, front overpass out of the area, height and location of the upper-air frontal zone, general motion direction of a frontal system and the levels in which a horizontal wind shear is located may be determined (Zhu *et al.*, 1984). Figure 5 shows a time-height chart of WPR horizontal wind speed at 2300 on 27 March 2010. As shown in Figure 5(a), around 2100, within the 800–1200 m level the wind direction changed from southeasterly to southwesterly, and to northwesterly at about 2300. The speeds of the prevailing northerly and northwesterly winds then continued to increase, and the layer was increasingly rising, with mean wind speed up to 15 m s^{-1} and the maximum speed nearly 19 m s^{-1} . This northerly airflow gradually extended to the upper atmosphere, generating strong winds in multiple periods until 2100 on 28 March (Figure 5(b)), when the high level was dominated by southwesterly and, finally, westerly wind. This suggested that the frontal system entered the area about 2200–2300 on 27 March: the surface was under the influence of a cold high pressure behind the front and the pressure was relatively lower

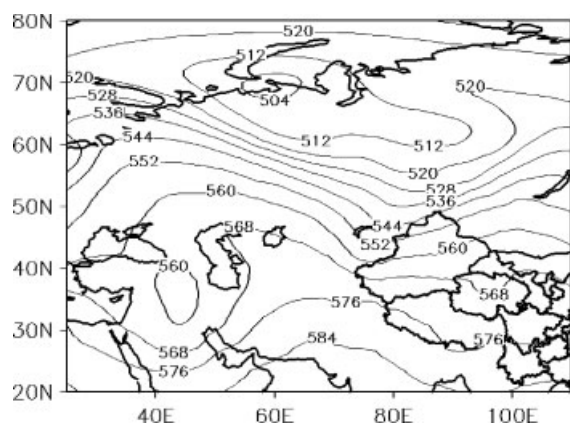


Figure 3. 500 hPa height field at 0800 on 28 March 2010.

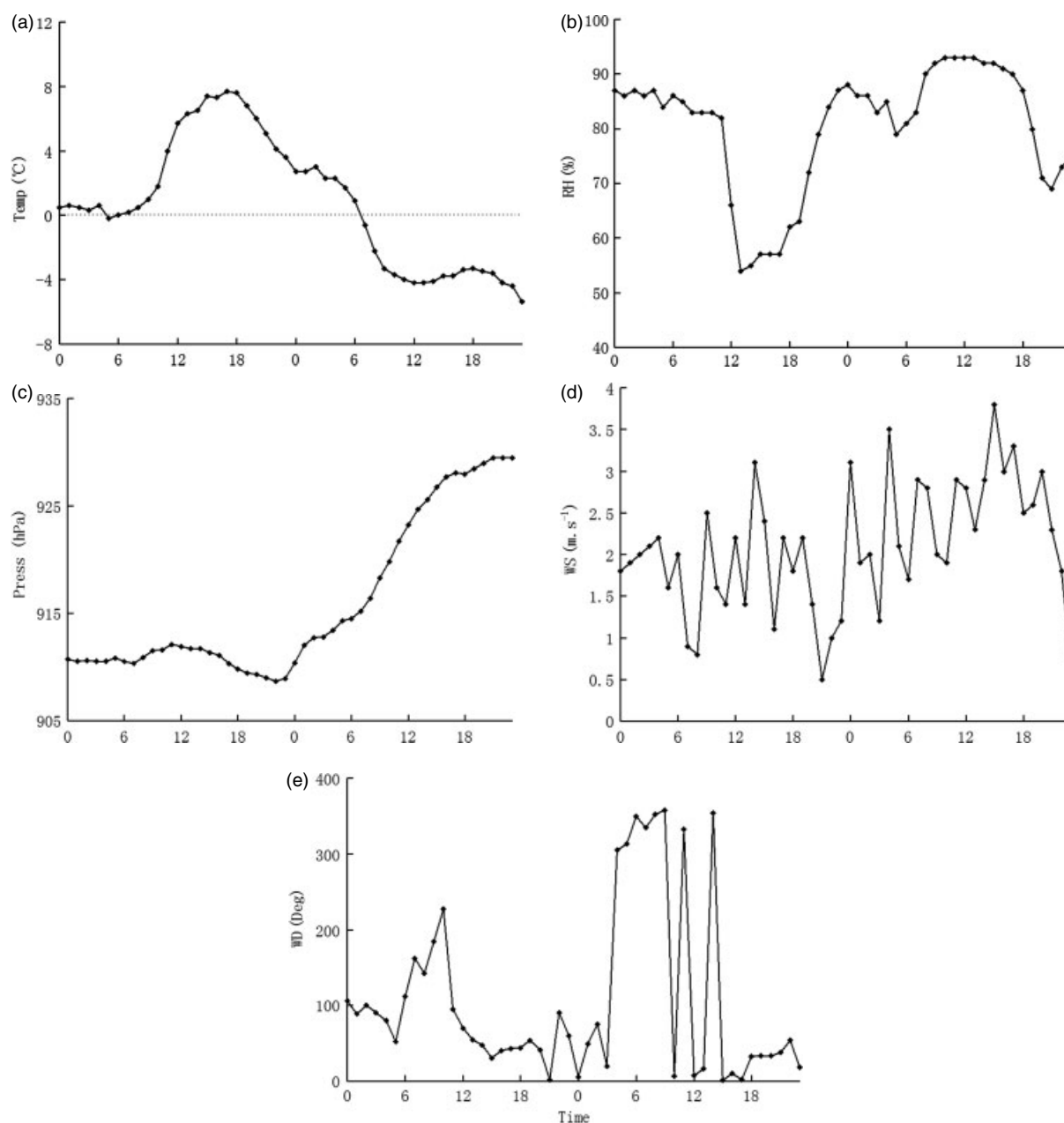


Figure 4. Changes of surface weather elements during snowstorm in 27–28 March 2010.

before the front. This sharp contrast in pressure gradient before and behind the front led to a strong northerly flow prevailing ahead of the cold high pressure at near surface level. At the same time, as shown in Figure 5(b), from the surface layer up to 5000 m, the wind changed counterclockwise with height, indicating that this layer was dominated by a strong cold advection, and that the area was being affected by the cold frontal system in this period. The ground observations from Urumqi Station showed that from 2200 on 27 March the surface pressure was increasing rapidly from 908.9 to 929.5 hPa at 2200 on 28 March. The temperature dropped from 7.7°C at 1700 (27 March) down to −6.8°C, while the surface wind speed increased rapidly at the same time. The FY-2 infrared satellite cloud image (Figure 6) at 2200 (27 March) clearly showed that the cold frontal system moved into the Xinjiang region at this hour. Therefore, the signal of the invading surface cold front captured by the wind-profiling radar was accurate. In this sense,

WPR data can be used as an important reference for determining the frontal nature and time of entry of a frontal system into a particular area.

Moreover, as shown in the wind profile chart (Figure 5(b)) on 28 March, a significant layer of discontinuity existed between 1500 and 5000 m, at which the wind direction changed with time. In other words, there was an evident shear line. Above the layer, the wind direction first changed from southeasterly to southwesterly and eventually to a westerly; below this, airflow was dominated by northwesterly and northerly wind layers, with the latter being gradually thickened. By around 2100 on 28 March, beneath 500 hPa, all winds changed to northerly and northwesterly, which showed a significant contrast between the circulation patterns in the upper atmosphere and those in the lower atmosphere in the snowstorm process. The shear line developing from a lower to a higher level leaves a footprint of the frontal zone as it passes

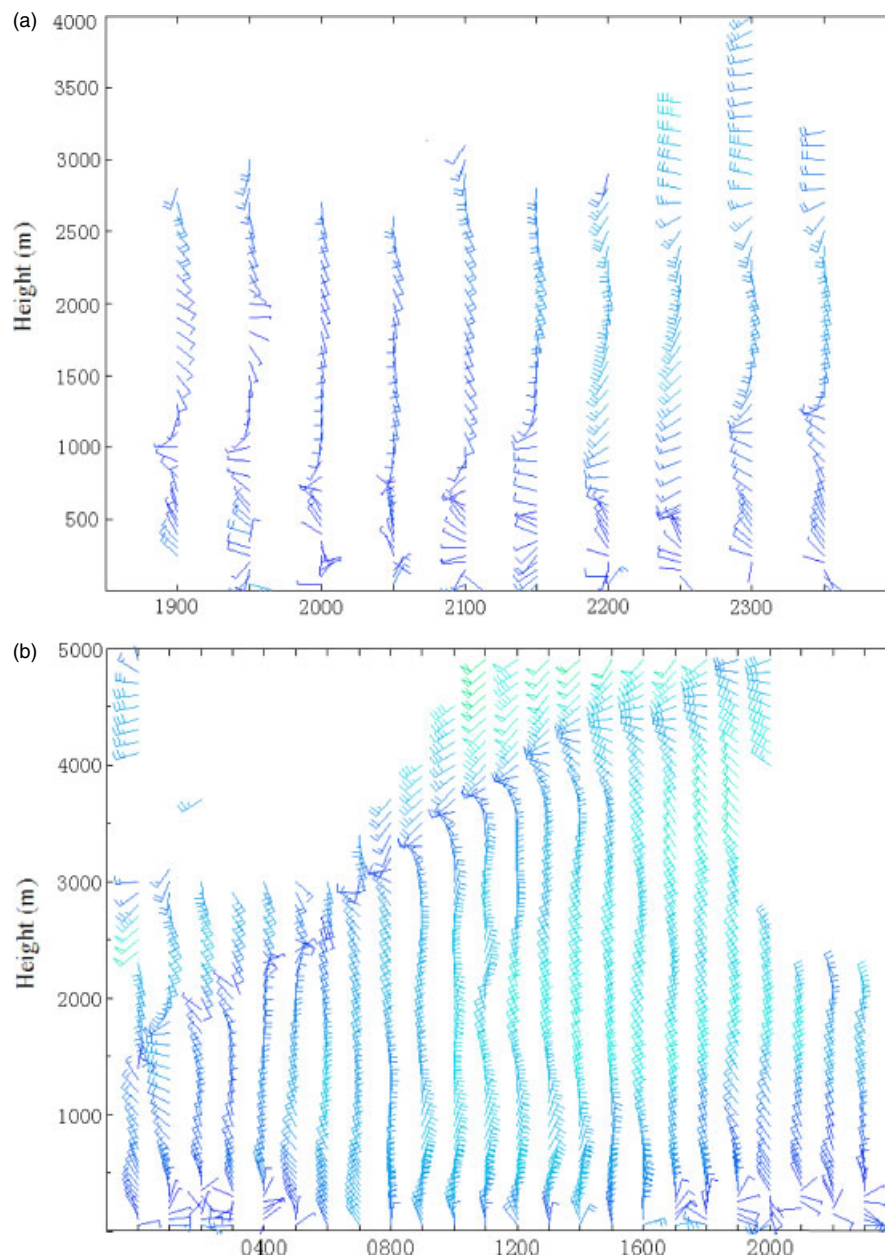


Figure 5. Wind profiles in 27–28 March 2010. This figure is available in colour online at wileyonlinelibrary.com/journal/met

the station, i.e. providing both position and height of the frontal zone when it passed. As shown in the figure, the frontal zone was located 1500 m above the station at 0000 on 28 March, and as the northerly wind intensified, the frontal zone was gradually pushed up. At around 2200 the cold front began to pass the station, reflecting that in the process the lower part of the cold front first affected the station, followed by the trough at upper levels. The weather situation at that time was that at 2300 on 27 March, Urumqi city was in front of the upper trough, while southwesterly and westerly winds prevailed in the upper atmosphere. However, by 0800 on 28 March the trough at the lower level had already passed the city, and the wind in lower atmosphere changed to a northwest direction. From the perspective of mid and upper levels, the city was still in front of the trough. Therefore, at this time the southwesterly winds still remained in the upper atmosphere. At about 2000, the upper trough moved out of the city and the high-level winds turned westerly and northwesterly.

The upper frontal zone, also referred to as an ‘isotherm ribbon’, was in parallel with the maximum thermal wind (Zhu *et al.*, 1984). Therefore, the direction of the upper frontal zone motion can be roughly determined by the direction of the maximum thermal wind. As shown by the time-height chart for wind profiles (Figure 5(b)), the maximum thermal wind was roughly along a northeast to southwest direction during the snowstorm process. Therefore, the cold front moved in the same direction.

5.2. WPR data application to derive thermal advection

Since WPR data have higher vertical resolutions, the detailed structure of the thermal advection distribution with height can be calculated from WPR data and the variation tendency in terms of the hydrostatic stability of atmosphere over a station can be further judged. Taking into account the standard atmospheric characteristics, the equation for calculating thermal

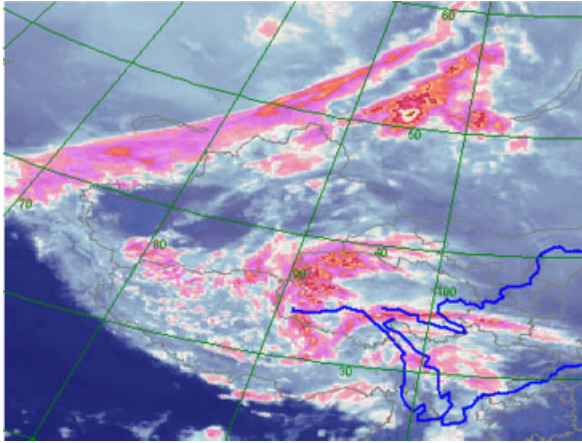


Figure 6. FY-2 infrared satellite cloud images at 2200 on 27 March 2010. This figure is available in colour online at wileyonlinelibrary.com/journal/met

advection from single-station WPR data is given as:

$$-V \bullet \nabla T = -\frac{Pf}{R_d} V \bullet (k \times \frac{\partial v}{\partial p}) \quad (1)$$

where, f is the Coriolis parameter and R_d the gas constant.

On the isobaric surfaces P_1 and P_2 ($P_1 > P_2$), the wind speeds and directions are (V_1, θ_1) and (V_2, θ_2) respectively. The full equation can be written as follows (Zhang *et al.*, 2007):

$$\begin{aligned} -V \bullet \nabla T &\approx -\frac{\bar{p}f}{R_d} \left(\frac{V_1 + V_2}{2} \right) \bullet \left(k \times \frac{V_1 - V_2}{\Delta p} \right) \\ &= -\frac{\bar{p}f}{R_d \Delta p} \bullet k \bullet (V_1 \times V_2) \\ &= -\frac{\bar{p}f}{R_d \Delta p} V_1 V_2 \sin(\theta_1 - \theta_2) \end{aligned} \quad (2)$$

where, $\Delta p = p_1 - p_2$, $\bar{p} = (p_1 + p_2)/2$.

Since WPR wind refers to a height in metres, a pressure-height conversion is required. Based on the known pressure-height correlation, its correlation with thermal advection on the same co-ordinates as the wind profile can be derived. Under standard atmospheric conditions, the correlation between geopotential height and atmospheric pressure is expressed as follows:

$$Z = 44331 \left[1 - \left(\frac{p}{1013.255} \right)^{0.1903} \right] \quad (3)$$

and the correlation between the height and the geopotential height is given below:

$$Z = \frac{9.80616(1 - 0.00259 \cos(2\varphi))(1 + \frac{h}{R_0})^2}{9.80665} \frac{R_0 h}{R_0 + h} \quad (4)$$

where R_0 stands for Earth radius and φ refers to local height.

According to the thermal wind principle, the nature and size of thermal advection can be determined from the wind direction changes with height. When the wind direction in a certain layer changes clockwise with height in the free atmosphere, a conclusion can be drawn that warm advection exists in the layer: if the wind direction changes counterclockwise with height, cold advection obviously exists in a given layer (Zhu *et al.*, 1984). As shown in Figure 5(b), the wind direction

during the entire snowstorm process turned counterclockwise from northwest to southwest and then to the southeast with height, meaning cold advection entered the layer. Based on calculations, Figure 7 presents a profile of thermal advection variations over time above Urumqi station on 28 March 2010. As shown in the figure, between 0000 and 2300, cold advection dominated beneath 2000 m, the passing cold front created the strong baroclinic instability that eventually led to the snowstorm.

Figure 8 shows WPR wind profiles shown with thermal advection profiles, when the cold front entered the area at 2300 on 27 March. As clearly shown by the wind barbs in the figure, at 2000 the wind direction changed counterclockwise from northwesterly to south-southeasterly below 1000 m, but above 2000 m it turned clockwise to a northerly wind, revealing that cold advection existed in the lower atmosphere and warm advection was in the upper atmosphere, just above the cold advection. From the calculated thermal advection profiles it is also discernable that when the cold front entered the area and cold advection dominated in the lower atmosphere below 1900 m, above which warm advection prevailed. As shown in the synoptic analysis, between 2200 and 2300, a cold

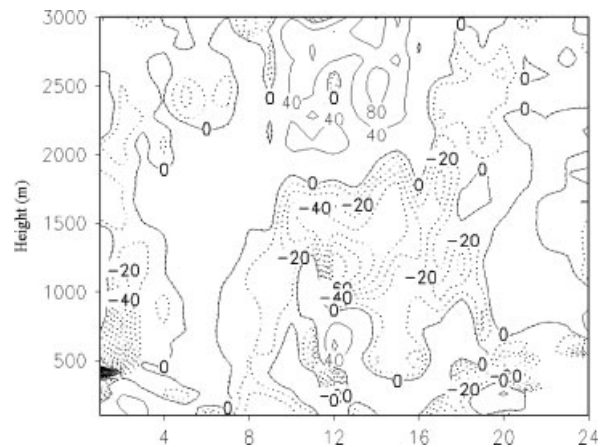


Figure 7. A time-height profile of thermal advection ($10^{-5} \text{ °C s}^{-1}$) on 28 March 2010.

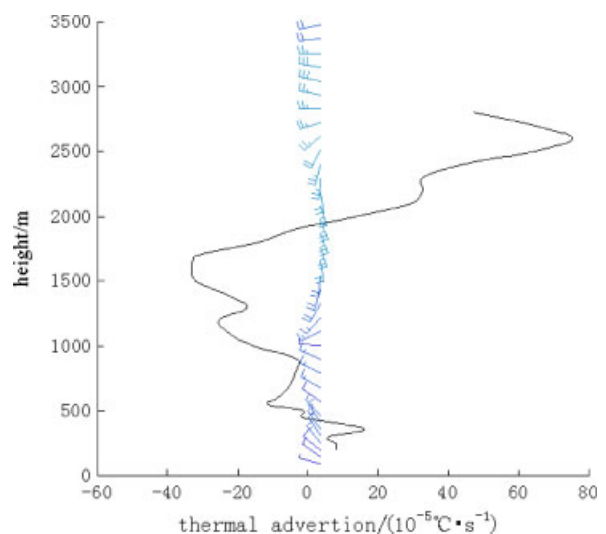


Figure 8. Wind profile overlapped with thermal advection profile at 2300 on 27 March. This figure is available in colour online at wileyonlinelibrary.com/journal/met

front began to impact the station, with the cold air in the lower atmosphere first passing by, as time went on, the cold air layer gained strength, gradually pushing the frontal zone up. According to quasi-geostrophic theory (Zhu *et al.*, 1984) thermal advection is one of the dynamic factors for large-scale vertical motion and development of a weather system, and therefore the thermal advection derived from the WPR data may serve as one of the bases for diagnosing weather pattern evolution.

5.3. Analysis of equivalent reflectivity factor Z_e

When a wind-profiling radar detects rain or snow in air, due to the fact that the ratio of the wavelength to the diameter of rain or snow particles is larger, and that in terms of radar wave scattering from the particles, the Rayleigh approach fits better, a common radar meteorological equation can be used to calculate the equivalent snowfall reflectivity, which is expressed as (Ruan *et al.*, 2002):

$$Z_e = \frac{1024 \times \ln 2 \times \lambda^2 \times R^2 \times L \times P_r}{\pi^3 \times P_t \times h \times G^2 \times \varphi \times \theta \times \left| \frac{m^2 - 1}{m^2 + 2} \right|^2}$$

$$P_r = SNR_0 \times P_n$$

$$P_n = K \times T_0 \times B \times N_f \quad (5)$$

where SNR_0 is the original signal to noise ratio, P_n represents the noise power, K is the Boltzmann constant ($1.38 \times 10^{-23} \text{ J K}^{-1}$), B is the bandwidth of the receiver, T_0 gives the absolute antenna temperature, N_f is the noise coefficient, λ provides the electromagnetic wavelength, R defines the distance to a target, L is the feeder power loss, P_r provides the echo power, π is a constant, P_t presents the transmitting peak power, G is the antenna gain, $\varphi \times \theta$ are the horizontal and vertical beam widths, $\left| \frac{m^2 - 1}{m^2 + 2} \right|^2$ is a dielectric constant (0.19) and Z_e denotes equivalent reflectivity factor.

In calculations, the noise power of the receiver P_n is obtained first, and based on the SNR value, the original signal to noise ratio SNR_0 is calculated without coherent accumulation in order to give true echo signals. The echo power P_r is then calculated, and, finally, the wind-profiling equivalent reflectivity factor Z_e is derived.

Figure 9 shows the time-height of the equivalent reflectivity factor Z_e on 28 March. As shown in the figure, both the onset and end of the snowstorms corresponded well with the equivalent reflectivity factor Z_e . The snowstorm occurred between 0416 and 1640, which just matched the red and yellow areas in the figure, i.e. Z_e has a large value zone indicating that when the snowstorm took place (rain) snow particle echoes were enhanced, increasing the equivalent reflectivity factor Z_e . When the snowfall stopped, back-scattering intensity weakened and Z_e decreased. Therefore, the onset and ending time of the snowstorms were consistent with Z_e .

Furthermore, during the sleet phase between 0416 and 0718, the height of the large Z_e value zone was found below 2000 m, suggesting that rain or snow particles mostly formed below 2000 m. During the snowfall process from 0718 to 1200, the Z_e value rapidly increased from near-surface to upper atmosphere and its top rose to 3000 m. This showed that this time ice particles formed at and below 3000 m, and snowfall intensity was greater, while the real weather situation then just matched

the above high-intensity period. As snowfall intensity was weakening, the height of large Z_e values zone began to drop, and snowfall ended at 1630. Accordingly, the Z_e value zone rapidly decreased from near-surface to the upper atmosphere. These analyses show that in a snowstorm process the equivalent reflectivity factor Z_e mainly reflects intensities of rain (snow) particles in back-scattering radar waves and they correlate well to the height of their formation, duration and snowfall intensity.

5.4. Vertical velocity analysis

Figure 10 shows time-height of vertical velocity from the wind-profiling radar in the snowstorm on 28 March 2010. During the precipitation, the distribution of power spectral density detected by the wind-profiling radar in the vertical direction contains both atmospheric and precipitation echoes, and the vertical velocity represented the composite value of both falling speed of the rain droplets (snowflakes) and atmospheric vertical velocity at that time (Wang *et al.*, 2010), an initial analysis is made on their composite velocities in this paper.

As shown in Figure 10, as the sleet began (at 0416), the composite vertical velocity from near surface up to the 2000 m level was rapidly increased at a rate of 2 m s^{-1} , showing a descending motion (negative/positive values are assigned to updraft/downdraft respectively in CFL-03 WPR definitions). As

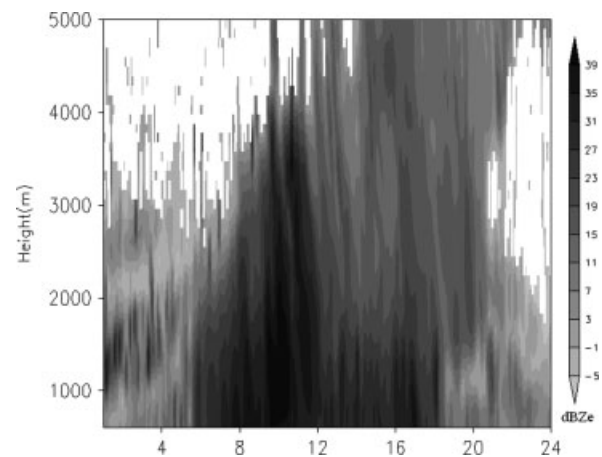


Figure 9. Evolution of the equivalent reflectivity factor Z_e in the snowfall process.

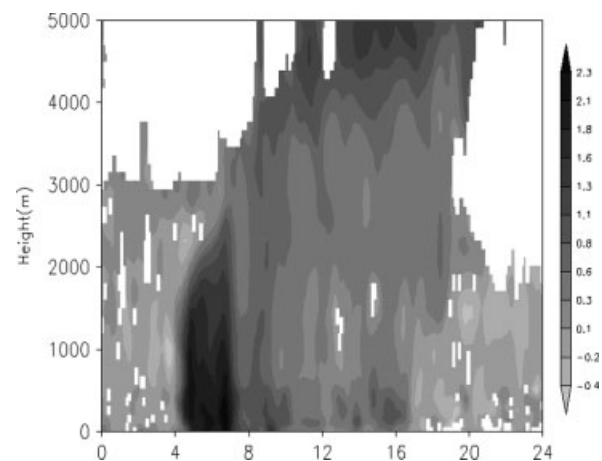


Figure 10. Vertical velocity variations in the snowfall process.

the detected composite vertical velocity mainly reflected falling motion of precipitation particles at that time, thus the large value zone in terms of the vertical velocity was consistent with the sleet process. When the sleet turned into snow (at 0718), the vertical velocity within the whole layer decreased rapidly in a range of 0.2–1.0 m s⁻¹. As the falling rate of snowflakes was less than that of rain droplets the radar-detected snowflake echo intensity was relatively weaker, hence the smaller composite vertical velocity values. However, when the snowstorm ended, a slight ascending motion was detected in the atmosphere accordingly.

6. Conclusions and discussion

The Urumqi Institute of Desert Meteorology under CMA launched an observational experiment on snowstorm with boundary layer wind-profiling radar (WPR) in Urumqi City in February to March 2010. In this paper, wind profiles from the experiment are used to compare with radiosonde data measured simultaneously to verify the accuracy of WPR data, which were then used to analyse the dynamic and thermal characteristics in the snowstorm process in Urumqi on 28 March 2010. Through the above study, the following preliminary conclusions can be made.

1. A Boundary Layer Wind-Profiling Radar system (CFL-03) can provide wind profiles in a higher temporal resolution. Comparing with synchronous radiosonde data, it is found that the WPR data are consistent with radiosonde data, and that the wind direction and velocity correlation coefficients in this study are 0.78 and 0.85 respectively.
2. Before the heavy snowfall, a surface wind shear already occurred. After outbreak of the event, the local weather was dominated by northwesterly and northerly winds, which were gaining strength rapidly, while temperature was dropping and air pressure was increasing.
3. From the analysis of the time-height images of wind profiles, it can be preliminarily determined that in this weather process the snowstorm was induced by the overpass of a cold front, and its arrival time was about 2200–2300 LST on 27 March 2010. The shear line that evolved from a lower to a higher level gave both height and location of the frontal zone. The cold front moved in a northeast-southwest direction.
4. The thermal advection and vertical pattern profiles derived from WPR data can be used as a basis for analysing changes of atmospheric hydrostatic stability and large-scale vertical motion. During the process, the wind changed counterclockwise with height. Under control by the cold advection, the overpass of the cold front created strong baroclinic instability that eventually led to the snowstorm.
5. When snowfall (rainfall) occurs, the atmospheric scattering mechanism will change accordingly. In this case, the equivalent reflectivity factor Z_e was more consistent with onset and end of the snowstorm, height of rain (snow) particles formation, and snowfall intensity.

It should be made clear that the above conclusions are simply based on an individual case study. In order to obtain universally meaningful findings from WPR data for addressing snowstorm weather in Urumqi, analyses of more snowstorm cases are required. Furthermore, this paper focuses on application of WPR data in weather process analysis, without an in-depth

analysis of particle properties derived from radar echoes. Future efforts will be made to separate rain droplet echoes from atmospheric echoes in a snowstorm event. Last, but not least, quantitative snowfall estimation may be explored on a trial basis, taking into account the relationship between radar echo intensity and snow particle size, as this is very useful for snowstorm weather analysis and forecasts.

Acknowledgements

This research was co-funded through the project for public good dedicated to the meteorological sector in China (GYHY201006012) and the National Basic Research Programme of China (2010CB951001). The authors thank Mrs. Ruan Zheng, a senior research fellow of the Chinese Academy of Meteorological Sciences, Mr. Ren Quan, Director of the Tianshan District Meteorological Bureau, Urumqi, and Mr. Zhao Keming, a meteorological engineer from the Xinjiang Meteorological Office for their provisions of valuable data and assistance.

References

- Angevine WM. 1997. Errors in mean vertical velocities measured by boundary layer wind profilers. *Journal of Atmospheric and Oceanic Technology* **14**: 565–569.
- Angevine WM, White AB, Avery SK. 1994. Boundary-layer depth and entrainment zone characterization with a boundary-layer profiler. *Boundary-Layer Meteorology* **68**: 375–385.
- Austin PM, Bemis A. 1950. A quantitative study of the bright band in radar precipitation echoes. *Journal of Meteorology* **7**: 165–171.
- Balsley BB, Ecklund WL, Carter DA, Riddle AC, Gage KS. 1988. Average vertical motions in the tropical atmosphere observed by a wind profiler on Pohnpei (7°N Latitude, 157°E longitude). *Journal of Atmospheric Science* **45**: 396–405.
- Balsley BB, Peterson VL. 1981. Doppler-radar measurements of clear air atmospheric turbulence at 1290 MHz. *Journal of Applied Meteorology* **20**: 266–274.
- Barth MF, Chadwick RB, van de Kamp DW. 1994. Data processing algorithms used by NOAA's wind profiler demonstration network. *Annales Geophysicae* **12**: 518–528.
- Bendel WB, Paton DD. 1981. A review of the effect of ice storm on the power industry. *Journal of Applied Meteorology* **20**: 1445–1449.
- Borga M, Anagnostou EN, Krajewski WF. 1997. A simulation approach for validation of a brightband correction method. *Journal of Applied Meteorology* **36**: 1507–1518.
- Braham RR Jr. 1983. The Midwest snow storm of 8–11 December 1977. *Monthly Weather Review* **111**: 253–272.
- Chen AY, Li CL, Chen XY. 1999. A comparison of heavy snow of formation in Spring and Winter. *Meteorology Monthly* **25**: 37–39.
- Cheng M, Collier CG. 1993. An objective method for recognizing and partially correcting brightband error in radar images. *Journal of Applied Meteorology* **32**: 1142–1149.
- Chilson PB, Ulbrich CW, Larsen MF, Perillat P, Keener JE. 1993. Observations of a tropical thunderstorm using a vertically pointing dual-frequency collinear beam Doppler radar. *Journal of Atmospheric and Oceanic Technology* **10**: 663–673.
- Cifelli R, Rutledge SA. 1998. Vertical motion, diabatic heating and rainfall characteristics in N. Australia convective systems. *Quarterly Journal of the Royal Meteorological Society* **124**: 1133–1162.
- Currier PE, Avery SK, Balsley BB, Gage KS, Ecklund WL. 1992. Use of two wind profilers in the estimation of raindrop size distribution. *Geophysical Research Letters* **19**: 1017–1020.
- Deshpande SM, Raj PE. 2009. UHF wind profiler observations during a tropical pre-monsoon thunderstorm – a case study. *Atmospheric Research* **93**: 179–187.
- Fukao S, Wakasugi K, Sato T, Morimoto S, Tsuda T, Hirota I, Kimura I, Kato S. 1985. Direct measurement of air and precipitation particle motion by very high frequency Doppler radar. *Nature* **316**: 712–714.
- Gage KS, Williams CR, Ecklund WL. 1996. Application of the 915 MHz profiler for diagnosing and classifying tropical precipitating cloud systems. *Meteorology and Atmospheric Physics* **59**: 141–151.

- Gossard EE, Wolfe DE, Moran KP, Paulus RA, Anderson KD, Rogers LT. 1998. Measurements of clear-air gradients and turbulence properties with radar wind profilers. *Journal of Atmospheric and Oceanic Technology* **15**: 21–342.
- Gu YX, Tao ZY. 1993. Analysis and application of UHF Wind Profiler Radar data during 1989–1990. *MesoScale Meteorology Corpus*. China Meteorology Press: Beijing; 194–201.
- Hashiguchi H, Fukal S, Tsuda T, Yamanaka MD, Harijono SWB, Wiryosumarto H. 1996. An overview of the planetary boundary-layer observations over equatorial Indonesia with an L-band clear-air Doppler radar. *Contributions to Atmospheric Physics* **69**: 13–25.
- He P. 2006. *Phased Array Wind Profiler Radar*. China Meteorology Press: Beijing; 2–3.
- He P, Ma Y, Ruan Z, Wang YC, Li CH, Cao XY. 2010. Study of thermal bubbles in the lower atmosphere based on the data detected using wind profiler radar. *Acta Meteorologica Sinica* **68**: 64–269.
- He P, Zhu XY, Ruan Z, Wu L, Yang XR, Ma SQ. 2009. Preliminary study on precipitation process detection using wind profiler radar. *Journal of Applied Meteorological Science* **20**: 465–470.
- Hermawan E, Tsuda T. 1999. Estimation of turbulence energy dissipation rate and vertical eddy diffusivity with MU radar RASS. *Journal of Atmospheric and Terrestrial Physics* **61**: 1123–1130.
- Hocking WK. 1983. On the extraction of atmospheric turbulence parameters from radar backscatter Doppler spectra I, Theory. *Journal of Atmospheric and Terrestrial Physics* **45**: 89–102.
- Hocking WK. 1985. Measurements of turbulent energy dissipation rates in the middle atmosphere by radar techniques: a review. *Radio Science* **20**: 1403–1422.
- Kuo Y-H, Donall EG, Shapiro MA. 1987. Feasibility of short-range numerical weather prediction using observations from a network of profilers. *Monthly Weather Review* **115**: 2402–2427.
- Larsen MF, Rottger J. 1987. Observation of thunderstorm reflectivities and Doppler velocities measured at VHF and UHF. *Journal of Atmospheric and Oceanic Technology* **4**: 151–159.
- Lothon M, Campistron B, Jacoby-Koaly S, Benecch B, Lohou F, Girard-Ardhuin F, Druilhet A. 2002. Comparison of radar reflectivity and vertical velocity observed with a scannable C-band Doppler radar and two UHF profilers in the lower troposphere. *Journal of Atmospheric and Oceanic Technology* **19**: 899–910.
- Maguire WB, Avery SK. 1994. Retrieval of raindrop size distributions using two Doppler wind profilers: model sensitivity testing. *Journal of Applied Meteorology* **33**: 1623–1635.
- May PT, Rajopadhyaya DK. 1999. Vertical velocity characteristics of deep convection over Darwin, Australia. *Monthly Weather Review* **127**: 1056–1071.
- Orr BW, Martner BE. 1996. Detection of weakly precipitating winter clouds by a NOAA 404-MHz wind profiler. *Journal of Atmospheric and Oceanic Technology* **13**: 570–580.
- Ralph FM. 1995. Using radar-measured radial vertical velocities to distinguish precipitation scattering from clear-air scattering. *Journal of Atmospheric and Oceanic Technology* **12**: 257–267.
- Rao TN, Rao DN, Raghavan S. 1999. Tropical precipitating systems observed with Indian MST radar. *Radio Science* **34**: 1125–1139.
- Ruan Z, Ge RS, Wu ZG. 2002. The reach of a method for the rain cloud structure with wind profiler. *Journal of Applied Meteorological Science* **13**: 170–179.
- Vaughan Z, Worthington RM. 2007. Inertia-gravity waves observed by the UK MST radar. *Quarterly Journal of the Royal Meteorological Society* **133**: 179–188.
- Wakasugi K, Mizutani A, Matsuo M. 1986. A direct method for deriving drop-size distribution and vertical air velocities from VHF Doppler radar spectra. *Journal of Atmospheric and Oceanic Technology* **3**: 623–629.
- Wang MZ, He Q, Wei WS, Zhao Y, Zhang GX. 2010. Observational study of wind profiles in gale area in Xinjiang. *Meteorological Science and Technology* **38**: 640–644.
- Wang DH, Liu CJ, Liu Y, Wei FY, Zhao N, Jiang ZN, Li Y, Chen GY, Wang YF, Shi XH, Xu XD. 2008. A preliminary analysis of features and causes of the snow storm event over the southern China in January 2008. *Acta Meteorologica Sinica* **66**: 405–422.
- Wang XL, Ruan Z, Ge RS, Chen ZR. 2010. A study of drop-size distribution in precipitation cloud from wind profile radar. *Plateau Meteorology* **29**: 498–505.
- Xin TE, He QS, Wei HR, Liu DW, Zhou GQ, Yang HQ, Shao DM. 2009. Observation and study of wind velocity variation with altitude over the EXPO land, Shanghai. *Plateau Meteorology* **28**: 127–135.
- Zhang GC, Jiao MY, Li YX. 2007. *Techniques and Methods of Contemporary Weather Forecast*. China Meteorology Press: Beijing; 78–99.
- Zhang Y, Wang X, Xu XD, Bian LG. 2004. Atmospheric profile synthesis detecting system and its application. *Meteorological Science and Technology* **32**: 263–268.
- Zhou LS, Li HH, Wang QC. 2000. Snowstorm process and snow disaster distribution in eastern pastoral areas of Qinghai-Xizang Plateau. *Plateau Meteorology* **19**: 450–458.
- Zhu QG, Lin JR, Shou SW. 1984. *Synoptic Meteorology Theory and Method*. China Meteorology Press: Beijing; 444–446.
- Zou H, Li P, Zhu JH, Ma SP, Li AG. 2007. Observational study on the wind from wind-profiler during HEST2007. *Plateau Meteorology* **26**: 1199–1207.